Comparison of different sensor thicknesses and substrate materials for the monolithic small collection-electrode technology demonstrator CLICTD

R. Ballabriga[a], J. Braach[a,1], E. Buschmann[a], M. Campbell[a], D. Dannheim[a], K. Dort[a,2,*], L. Huth[b], I. Kremastiotis[a], J. Kröger[a,3], L. Linssen[a], M. Munker[c], W. Snoeys[a], S. Spannagel[b], P. Švihra[a], T. Vanat[b]

[a] *CERN, Geneva, Switzerland*
[b] *Deutsches Elektronen-Synchrotron DESY, Notkestr. 85, 22607 Hamburg, Germany*
[c] *University of Geneva, Geneva, Switzerland*

Abstract

Small collection-electrode monolithic CMOS sensors are attractive candidates for large-area tracking detectors. The small collection-electrode design allows for a minimisation of the input capacitance to obtain a high signal-to-noise ratio and a small power consumption. However, achieving a sizeable depleted volume is challenging in this design. Typically, a high-resistivity epitaxial layer grown on top of a low-resistivity substrate is used to fabricate these devices, which confines the depletion and the active sensor volume to the thickness of the epitaxial layer. In this paper, the active sensor depth is investigated in the monolithic small collection-electrode technology demonstrator CLICTD. Charged particle beams are used to study the charge collection properties and the performance of CLICTD sensors with different thicknesses both for perpendicular and inclined particle incidence. Using a high-resistivity substrate instead of an epitaxial layer allows the depleted volume to evolve further in depth. CLICTD sensor fabricated on a high-resistivity Czochralski substrate are thus investigated and a potential for large performance improvements is found regarding the spatial and time resolution as well as the hit-detection efficiency. Most importantly, the depth of the sensitive volume is mapped out by means of grazing angle measurements for both substrate materials and a more than twofold increase for the high-resistivity Czochralski substrate is found.

Keywords: High-resistivity Czochralski silicon, Inclined particle tracks, Monolithic silicon sensor, Small collection-electrode design

1. Introduction

In monolithic CMOS sensors the readout electronics are integrated into the active sensor volume, which offers the potential for fine pixel pitches and a small material content. The devices are particularly interesting for large-scale production efforts by profiting from the commercial CMOS industry. Monolithic sensor designs featuring a small collection electrode benefit from a reduced capacitance, which enables an improvement in signal-to-noise ratio and reduced power consumption [1]. Several sensors have been fabricated in a modified 180 nm CMOS imaging process implementing the small collection-electrode design with a 25 - 30 µm high-resistivity epitaxial layer on a low-resistivity substrate, such as the ALPIDE [2], (Mini-)MALTA [3], FASTPix [4] and CLICTD [5] sensors.

They have exhibited promising results regarding radiation tolerance, a time resolution down to hundreds of picoseconds, a spatial resolution of a few micrometers and full efficiency over a wide threshold range of several hundred electrons.

Although sensor optimisations enable a full lateral depletion [6] in the small collection-electrode design, the sensors are only partially depleted in depth. The active sensor depth, from which charge carriers contribute to the signal, extends further than the depletion depth but is limited by the thickness of the epitaxial layer due to the short charge carrier lifetime in the low-resistivity substrate. To extend the bounded depletion and active sensor depth, high-resistivity substrate materials are investigated, which promise a higher signal due to a larger sensitive volume. In this document, a high-resistivity Czochralski substrate as alternative wafer material is assessed, which has already proven to improve efficiency after irradiation in the small collection-electrode design [7].

An in-depth comparison of 40 - 300 µm thick sensors in the original epitaxial-layer design with 100 µm thick high-resistivity Czochralski sensors is presented for the CLICTD technology demonstrator. To this end, the performance and charge sharing characteristics of different CLICTD sensors are studied using charged particle beams with perpendicular and inclined incidence relative to the sensor surface. Most notably, in-pixel studies are pre-

* Corresponding author
Email address: `katharina.dort@cern.ch` (K. Dort)
1 Also at University of Hamburg, Germany
2 Also at University of Giessen, Germany
3 Also at University of Heidelberg, Germany

sented that allow for a two-dimensional mapping of charge collection properties. The effective active sensor volume is determined as well by employing the grazing angle technique [8] for the different sensor thicknesses and materials.

2. The CLICTD Sensor

The CLICTD sensor features a matrix of 16×128 detection channels with a size of $300\,\mu\text{m} \times 30\,\mu\text{m}$ in column × row direction. Each channel is segmented along the column direction into 8 sub-pixels with a size of $37.5\,\mu\text{m} \times 30\,\mu\text{m}$. The following section gives a brief overview of the main features of the CLICTD sensor. Additional details can be found in [5] and [9].

2.1. Sensor Design

The CLICTD sensor is fabricated in a modified 180 nm CMOS imaging process [6] using two different pixel flavours, as shown schematically in Fig. 1. The sensor is characterised by a small n-type collection electrode on top of a 30 µm thick high-resistivity (few kΩcm) epitaxial layer, that is grown on a low-resistivity ($\sim 10^{-2}\,\Omega\,\text{cm}$) p-type substrate. The on-channel front-end electronics are shielded by p-wells at the pixel edges. A low-dose n-type implant below the p-wells allows for full lateral depletion of the epitaxial layer [6]. In the second pixel flavour, the n-implant is segmented at the pixel edges, which causes an increase in the lateral electric field. As a consequence, an accelerated charge collection and reduced charge sharing is achieved with this flavour. In the CLICTD sensor, the segmentation is only introduced in the column direction. In the row direction, a high degree of charge sharing is desired in order to improve the spatial resolution.

A reverse bias voltage is applied to nodes in the p-wells and the substrate. The bias voltage at the p-wells is limited to -6 V to prevent breakdown of the on-channel NMOS transistors [10].

CLICTD sensors with different thicknesses were produced using backside grinding. The total device thickness ranges from 40 µm to 300 µm, including a metal stack of approximately 10 µm on top of the sensor [11].

High-resistivity Wafer Material. The size of the depleted volume is limited by the thickness of the high-resistivity epitaxial layer. To increase the depleted volume, an alternative wafer material is studied, which consists of high-resistivity (few kΩ cm) p-type Czochralski silicon [7]. The implants are implemented directly on the 100 µm thick Czochralski substrate and no additional epitaxial layer is grown on top. The advantages of the high-resistivity wafer material are twofold: Firstly, the isolation between p-well and substrate bias nodes is improved, allowing for a larger difference of the two voltages. Secondly, the depletion can evolve further in depth owing to the larger size of the high-resistivity volume.

2.2. Analogue and digital front-end

Each sub-pixel has an analogue front-end that consists of a voltage amplifier connected to a discriminator, where an adjustable detection threshold is compared to the input pulses. Effective threshold variations are corrected using a 3-bit threshold-tuning DAC.

The discriminator output of the eight sub-pixels in a detection channel are combined with a logical *OR* in the on-channel digital front-end. The binary hit pattern of the sub-pixels is recorded as well as the 8-bit Time-of-Arrival (ToA) and the 5-bit Time-over-Threshold (ToT) for time and energy measurements, respectively. As a consequence of combining the sub-pixel discriminator outputs, the ToA is set by the earliest sub-pixel timestamp and the ToT is determined by the number of clock cycles in which at least one sub-pixel is above the detection threshold.

For all measurements, no conversion from ToT to physical units is applied, since the conversion was found to have a limited precision owing to non-linearities in the analogue front-end [5].

2.3. Sensor operation

The front-end and operation settings were optimised in laboratory studies detailed elsewhere [5, 9]. Most importantly, for each sensor a minimum operation threshold is defined as the lowest possible threshold at which a noise free operation ($< 1 \times 10^{-3}$ hits/sec for the full pixel matrix) is achievable. It should be noted that measurements below the minimum operation threshold are nevertheless feasible, since small noise contribution can be tolerated.

The difference between the substrate and p-well bias voltages is limited by the punch-through between the two nodes. Whereas this requirement constraints the difference to a few volts for sensors with epitaxial layer, for the high-resistivity Czochralski sensors, the difference can easily exceed tens of volts. For the sensors with epitaxial layer, a high substrate bias voltage has a negligible impact, since the depletion depth is limited by the thickness of the epitaxial layer itself. Therefore, the bias voltage is fixed to -6 V/-6 V at the p-well/substrate nodes for measurements presented in the following sections. For the high-resistivity Czochralski sensors, the depletion region can evolve further into the substrate, thus justifying measurements with increased substrate bias voltage.

Front-End Optimisation. The CLICTD front-end is optimised for sensors with a 30 µm epitaxial layer. Sensors fabricated on high-resistivity Czochralski substrates are subject to a considerable leakage current, if the difference between p-well and substrate voltage exceeds 5 V. The leakage current can saturate the first stage of the readout electronics, which renders parts of the pixel matrix insensitive to incoming particles. To counteract the saturation, the front-end settings are adapted such that a faster return to baseline at the input node is achieved. With these settings, the sensor can be operated up to -20 V substrate bias

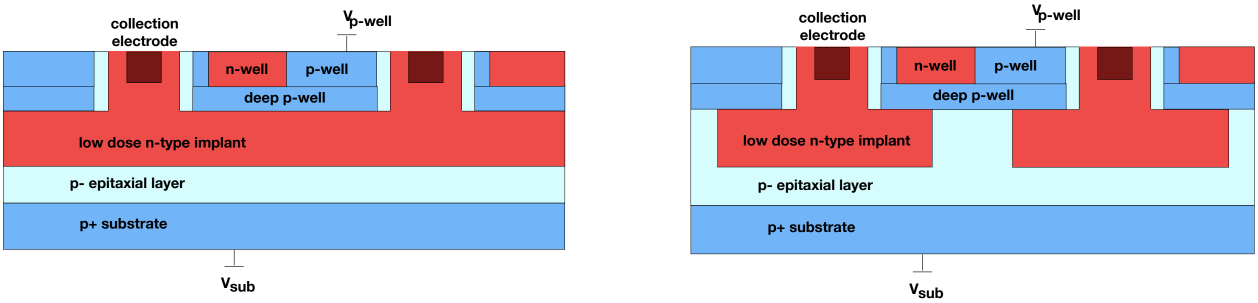

(a) Continuous n-implant (b) Segmented n-implant

Figure 1: Schematics of the CLICTD pixel design for the pixel flavour with (a) continuous and (b) segmented n-implant. Not to scale.

voltage before any saturation effects set in. However, the adaptations reduce the signal gain, which leads to coarser steps in the threshold settings and a larger minimum operation threshold, since the front-end is operated in conditions it was not optimised for. The higher thresholds have important implications for the sensor performance, as presented in Section 4.

3. Test-Beam and Analysis Setup

Test-beam measurements were performed at the DESY II Test-Beam Facility [12] using a MIMOSA-26 telescope [13] equipped with an additional Timepix3 [14] plane for improved track-time resolution, as schematically depicted in Fig. 2. The beam consisted of 5.4 GeV electrons and data for different incidence angles between the beam and the sensor surface was recorded. To this end, the Device-Under-Test (DUT) was mounted on a rotation stage to allow for inclinations relative to the beam axis.

Two different telescope plane spacings were used to optimise the tracking performance for the respective measurements: For measurements with perpendicular incidence between the beam and the sensor surface, the innermost telescope planes are as close as physically possible to the DUT. When the DUT is rotated, the telescope planes are adjusted such that the DUT can be tilted to $\leq 70^{\circ}$ without touching the telescope planes.

A trigger signal is provided by the AIDA Trigger Logic Unit (TLU) [15] consisting of a coincidence between two scintillators in front of the first telescope plane. The EUDAQ2 data acquisition framework is used to control and read out the telescope and the DUT [16].

3.1. Reconstruction and Analysis

The software framework Corryvreckan [17, 18] is used to perform offline reconstruction and analysis of the test-beam data. Individual events are defined by CLICTD readout frames. The Timepix3 hit timestamp and the TLU trigger timestamp associated to MIMOSA-26 hits determine their allocation to a specific event by requiring that the timestamp is within a CLICTD frame. The subsequent analysis proceeds on an event-by-event basis.

For each telescope plane and the DUT, adjacent pixel hits are combined into clusters and the cluster position is calculated by a ToT-weighted centre-of-gravity algorithm. For the CLICTD sensor, the cluster position in row direction is corrected using the η-formalism to take non-linear charge sharing between pixel cells into account [19]. In addition, *split clusters* are considered for measurements with rotated DUT i.e. a gap of one pixel is permitted between pixel hits in a cluster.

Track candidates are formed from clusters on each of the seven telescope planes. For track fitting the General Broken Lines (GBL) formalism [20] is used to account for multiple scattering in the material. The telescope alignment is performed by minimising the track χ^2 distribution. Tracks with a χ^2 per degree of freedom larger than three are discarded. The telescope track resolution at the position of the DUT is 2.4 µm for the close telescope plane spacing and 5.6 µm for the wide rotation configuration, as estimated from analytical calculations based on [21, 22].

A reconstructed track is associated with a CLICTD cluster by requiring a spatial distance of less than 1.5 pixel pitches between the global track intercept position on the DUT and the reconstructed cluster position as well as a track timestamp within the same CLICTD frame as the cluster. It has been verified that the spatial cut is sufficiently large even for the worse track resolution at the position of the DUT in the wide telescope-plane configuration. Clusters adjacent to the edge of the pixel matrix are rejected to prevent edge effects. The following observables are considered to characterise the DUT:

Cluster size. The cluster size is defined as the number of pixels in a given cluster. Correspondingly, the cluster size in column/row direction is given by the projection of the cluster size onto the respective axis. The systematic uncertainty on the cluster size arises from uncertainties in the threshold calibration, as detailed in [5]. At the minimum operation threshold, the systematic uncertainty evaluates to ± 0.01 for the mean cluster size and the statistical uncertainty is of the order of 10^{-4}.

Hit detection efficiency. The hit detection efficiency is calculated as the number of associated tracks divided by the

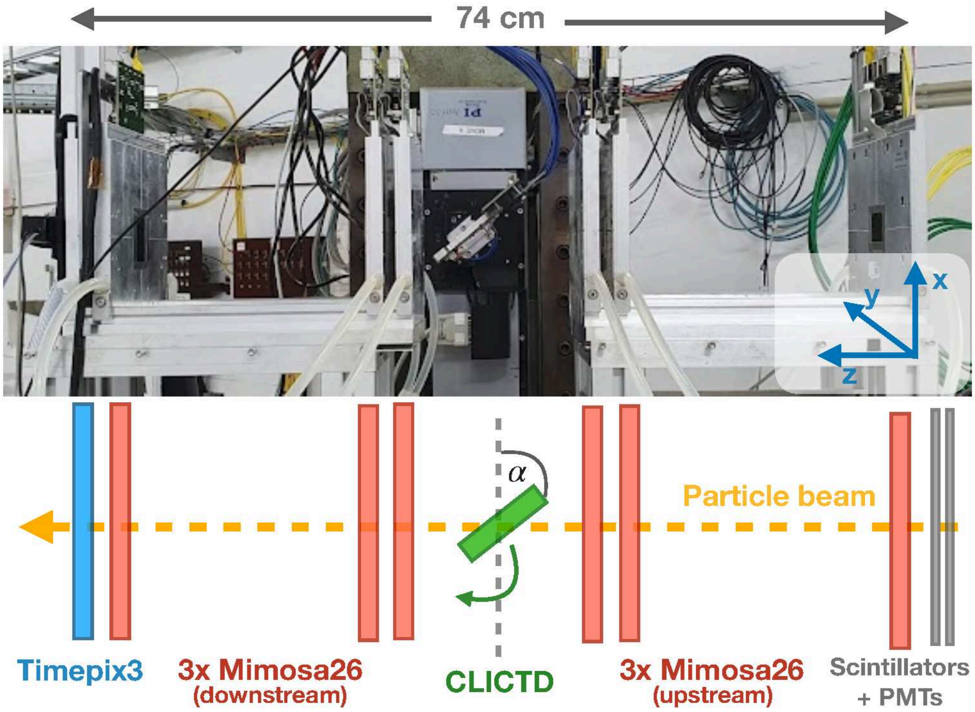

Figure 2: Test-beam setup with a rotated DUT

total number of tracks. The considered tracks are required to pass through the acceptance region of the DUT, excluding one column/row at the pixel edge as well as masked pixels and their direct neighbours. The statistical uncertainty is calculated using a Clopper-Pearson interval of one sigma [23] and the systematic uncertainty arises from the threshold calibration as mentioned above.

Spatial resolution. The unbiased spatial residuals are calculated as the difference between the reconstructed cluster position and the track intercept on the DUT. The RMS of the central $3\,\sigma$ of the distribution is extracted and the spatial telescope track resolution is quadratically subtracted, which yields the spatial resolution of the DUT.

At the minimum operation threshold, the statistical uncertainty on the spatial resolution is of the order of 10^{-2}µm. The systematic uncertainties result from uncertainties in the telescope single-plane resolution given in [22]. In addition, the plane positions in z-direction are shifted independently by ±1 mm and the calculation of the track resolution at the position of the DUT is repeated. Propagating the deviations to the spatial resolution yields an uncertainty of ±0.1 µm. The propagated threshold uncertainty evaluates to ±0.1 µm as well and the total systematic uncertainty is given by the quadratic sum of the two.

Time resolution. Similar to the spatial residuals, the time residuals are defined as the difference between the DUT timestamp and the track timestamp. Signal-dependent time-walk effects are corrected by exploiting the ToT information. To this end, the mean time difference between the DUT and the track timestamp are subtracted for each ToT bin separately. After correction, the RMS of the central $3\,\sigma$ of the time residuals distribution is calculated and the track time resolution of 1.1 ns [24] is quadratically subtracted.

The statistical uncertainties are of the order of 0.01 ns. The systematic uncertainties are composed of the threshold uncertainty evaluating to ±0.1 ns and sub-pixel by sub-pixel variations. To quantify the latter, the analysis is repeated for every sub-pixel in a detection channel individually and the spread of the time resolution is used to define the systematic uncertainty, which yields ±0.1 ns at the minimum operation threshold.

Studies with inclined particle tracks. The inclination angle of the DUT with respect to the beam is taken from the alignment procedure. The angle agrees with the nominal rotation angle set for the rotation stage apart from a constant offset. It was confirmed that the alignment has converged by manually modifying the plane orientation by $\pm0.5°$ and repeating the alignment. A deviation of less than $\pm0.01°$ is found with respect to the initial alignment.

4. Performance for Perpendicular Particle Tracks

First, measurement results for perpendicular beam incidence are presented. Here, CLICTD sensors with different thicknesses and wafer materials are compared for the two

Thickn. [µm]	**Mat.**	**Fl.**	**Thd.** [e]	**CS**
300	Epi	C	139^{+4}_{-5}	1.99 ± 0.01
100	Epi	C	136^{+4}_{-5}	1.94 ± 0.01
50	Epi	C	140^{+4}_{-5}	1.91 ± 0.01
40	Epi	C	138^{+4}_{-5}	1.86 ± 0.01
300	Epi	S	136^{+4}_{-5}	1.82 ± 0.01
100	Epi	S	140^{+4}_{-5}	1.81 ± 0.01
50	Epi	S	131^{+4}_{-5}	1.83 ± 0.01
40	Epi	S	130^{+4}_{-5}	1.73 ± 0.01
100	Cz	S	151^{+4}_{-5}	2.36 ± 0.01

Table 1: Mean cluster size (CS) at the minimum operation threshold (Thd.) for both pixel flavours (Fl.), different sensor thicknesses (Thickn..) and wafer materials (Mat.). C - continuous n-implant, S - segmented n-implant, Epi - epitaxial layer, Cz - high-resistivity Czochralski substrate.

different pixel flavours. A comparison of the pixel flavours themselves can be found elsewhere [5].

4.1. Cluster Size

Comparing the cluster size of different sensors is sensitive to the total amount of induced charge and its distribution among adjacent pixel cells. The mean cluster size for the two pixel flavours as a function of the detection threshold is presented in Fig. 3 and the mean size at the minimum detection threshold is listed in Table 1. The shaded band represents the uncertainties discussed in the previous section.

For both pixel flavours, the mean cluster size is the same within the uncertainties for sensor thicknesses between 50 µm and 300 µm. The results imply that only a fraction of the low-resistivity substrate is removed, from which no charge carrier contribution to the signal is expected. Thus, thinning the sensor to 50 µm still leaves the active sensor material intact.

On the other hand, the mean cluster size for the 40 µm thick sensor is reduced by approximately 10 % at the minimum operation threshold, which implies removal or damage to the active sensor volume. As the 40 µm thick sensor consists of approximately 10 µm of metal layers and 30 µm sensor material, it can be assumed that the substrate is fully removed. Damage to the epitaxial layer by the thinning procedure [25] is expected to affect the signal as well, which results in a lower cluster size.

The decrease in mean cluster size is more severe for the pixel flavour with segmented n-implant (cf. Fig. 3b), which is consistent with the smaller charge sharing expected for this flavour. A high degree of charge sharing leads to the distribution of the total signal to several adjacent pixel cells, thus reducing the amount of signal per pixel. In particular, charge carriers generated at the lower border of the active sensor region are subject to intense charge sharing, since their longer propagation path allows for a stronger contribution of diffusion processes. If the induced signal on a given pixel is not enough to surpass the threshold, the charge carriers that propagated to this cell are effectively lost (sub-threshold effect). Therefore, this phenomenon is particularly important for the flavour with continuous n-implant and affects mostly charge carriers from the lower part of the active sensor volume. A removal of this volume is thus less severe, since a fraction of charge carriers are anyway lost due to sub-threshold effects. The stronger concentration of charge carriers for the pixel flavour with segmented n-implant mitigates the charge-sharing-induced signal loss and this flavour is consequently more sensitive to the thinning procedure.

The mean cluster size for a 100 µm thick sensor fabricated on a high-resistivity Czochralski substrate is also shown in Fig. 3b. At the minimum threshold, the mean cluster size is increased by approximately 20 % compared to sensors with epitaxial layer, which is indicative of a higher signal and consequently a larger active sensor volume.

The in-pixel representation of the cluster size for the two different materials is depicted in Fig 4. This representation allows for a comparison of the cluster size as a function of the particle incident position within the pixel cell by folding data from a full CLICTD pixel matrix into a single cell. The largest clusters originate from the pixel corners owing to geometrical effects and the low electric field in this region resulting in a high contribution from charge carrier diffusion. For the sensor fabricated on high-resistivity Czochralski substrate, the cluster size is larger regardless of the incident position. Especially in the pixel centre, the map exhibits mean cluster size values well above one, even though the lowest degree of charge sharing is expected from this region.

The depletion region within the high-resistivity Czochralski sensor is not expected to extend to the sensor backside at a bias voltage of -6 V/-6 V, which still limits the active sensor depth. An increase in substrate bias voltage, increases the depletion depth and therefore also affects the active depth, as illustrated in Fig. 5, where the mean cluster size as a function of the substrate bias voltage is displayed for the pixel flavour with segmented n-implant. The p-well voltage is fixed to -6 V and a higher detection threshold of 226 e is applied to the sensor due to the different front-end operation settings as explained before.

4.2. Efficiency

The hit detection efficiency is closely related to the maximum single-pixel charge (*seed charge*) in a cluster and is thus correlated to the total signal and the degree of charge sharing. The efficiency is determined as a function of the detection threshold as presented in Fig. 6 for both pixel flavours. While efficiencies well above 99 % are achieved at low detection thresholds, the efficiency deteriorates for values greater than 500 e, since all single-pixel signals in a cluster can fall below the detection threshold.

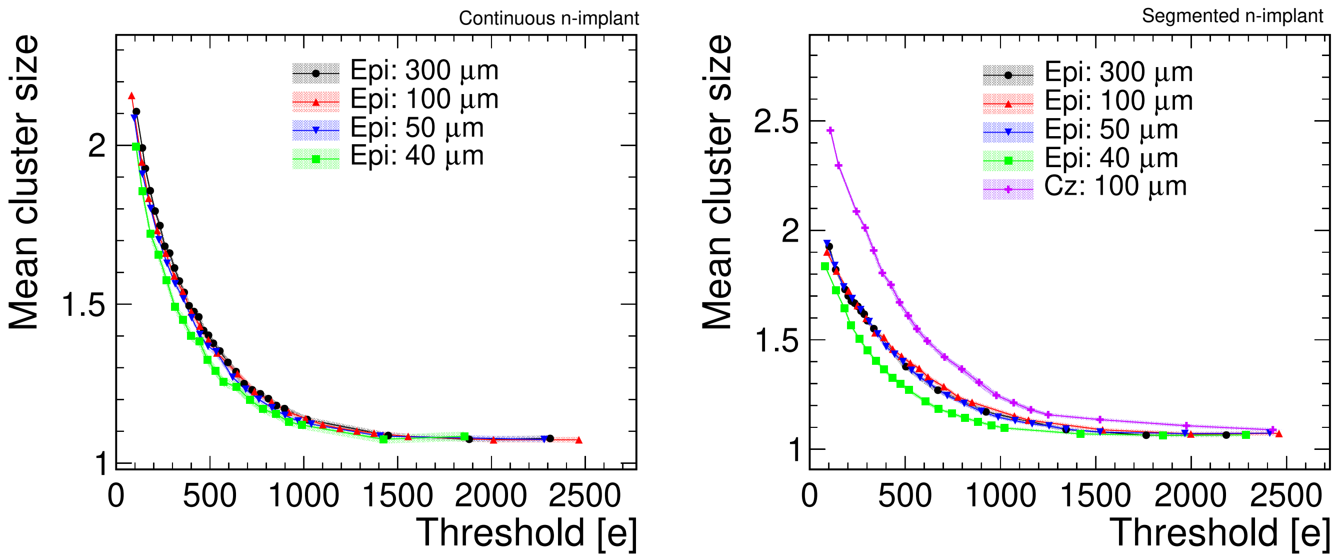

(a) Continuous n-implant

(b) Segmented n-implant

Figure 3: Mean cluster size as a function of the detection threshold using sensors with different sensor thicknesses and wafer materials for the pixel flavour with (a) continuous and (b) segmented n-implant using a bias voltage of -6 V/-6 V at the p-well/substrate.

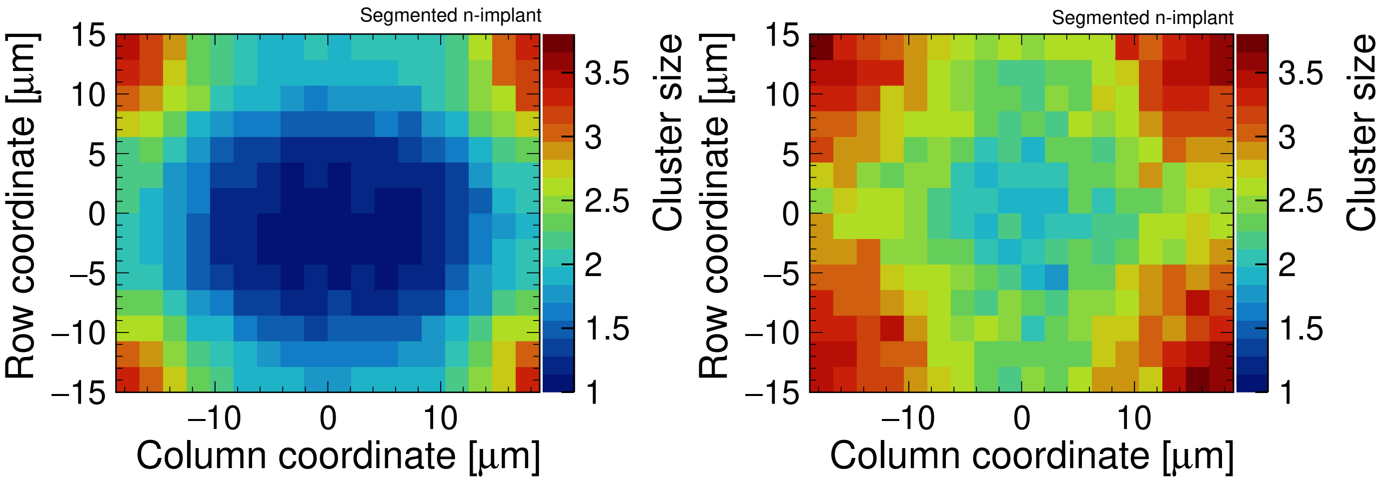

(a) Epitaxial layer

(b) High-resistivity Czochralski

Figure 4: In-pixel representation of the total cluster size at the minimum detection threshold for a sensor with (a) epitaxial layer and (b) high-resistivity Czochralski substrate. Both sensors have a segmented n-implant and are biased at -6 V/-6 V at p-wells/substrate.

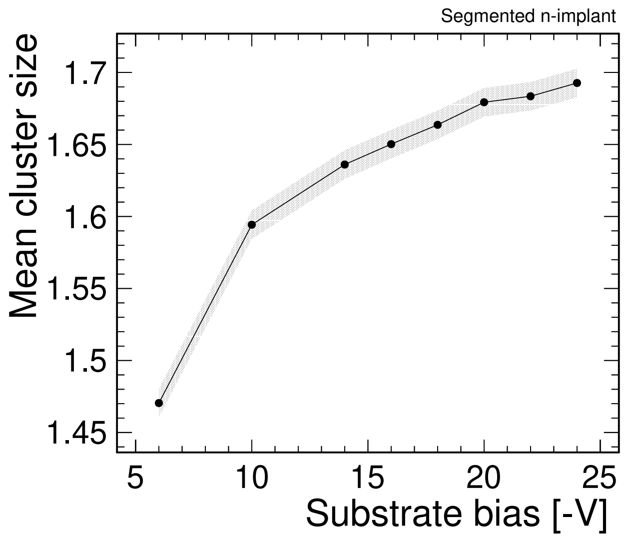

Figure 5: Mean cluster size as a function of the substrate bias voltage at a threshold of 226 e for a high-resistivity Czochralski sensor with segmented n-implant. The p-well voltage is fixed to -6 V.

Thickn. [µm]	**Mat.**	**Fl.**	**Thd.** [e]	**SR (row)** [µm]
300	Epi	C	139^{+4}_{-5}	4.6 ± 0.2
100	Epi	C	136^{+4}_{-5}	4.6 ± 0.2
50	Epi	C	140^{+4}_{-5}	4.6 ± 0.2
40	Epi	C	138^{+4}_{-5}	4.9 ± 0.2
300	Epi	S	136^{+4}_{-5}	4.6 ± 0.2
100	Epi	S	140^{+4}_{-5}	4.5 ± 0.2
50	Epi	S	131^{+4}_{-5}	4.6 ± 0.2
40	Epi	S	130^{+4}_{-5}	4.8 ± 0.2
100	Cz	S	151^{+4}_{-5}	3.9 ± 0.2

Table 2: Spatial resolution (SR) in row direction at the minimum operation threshold (Thd.) for both pixel flavours (Fl.), different sensor thicknesses (Thickn.) and wafer materials (Mat.). C - continuous n-implant, S - segmented n-implant, Epi - epitaxial layer, Cz - high-resistivity Czochralski substrate.

For high thresholds, inefficient regions start to form at the pixel borders, as illustrated in Fig. 7a, where the in-pixel efficiency is shown at a threshold of 1950 e for a 300 µm thick sensor with segmented n-implant and epitaxial layer. As the diffusion of charge carriers to neighbouring pixels is enhanced at the edges, a smaller seed signal and consequently a lower efficiency occurs in these regions.

For the 40 µm thick sensors, the high efficiency plateau is noticeably reduced. In agreement with the smaller cluster size observed in the previous section, the degraded efficiency indicates an overall reduction in signal compared to the thicker sensors. These results support the assumption of a smaller active depth due to the removal of sensitive sensor volume. The degradation in efficiency is less severe for the pixel flavour with continuous n-implant due to sub-threshold losses as discussed above. The efficiency of 100 µm and 50 µm thick sensors is less affected, which confirms that primarily passive material was removed.

The sensor fabricated on high-resistivity Czochralski substrate exhibits a larger efficiency at high detection thresholds compared to sensors with epitaxial layer as a direct consequence of the higher signal. The in-pixel representation of the efficiency is depicted in Fig. 7b at a detection threshold of approximately 1950 e and confirms that the efficiency is larger especially in the pixel edges, where the highest degree of charge sharing is expected.

The impact of the substrate voltage on the efficiency is shown in Fig. 8 for a high-resistivity sensor with segmented n-implant at a threshold of 1570 e. As this threshold is about one order of magnitude higher than the minimum operation threshold, a significant reduction in efficiency is measured. However, the efficiency loss is less severe for operations with a high substrate bias voltage, since a larger seed signal is expected from the increased depletion depth. The efficiency thus increases by about 5 % between -6 V and -20 V substrate bias voltage.

4.3. Spatial Resolution

The spatial resolution in row direction as a function of the detection threshold is presented in Fig. 9 for both pixel flavours and the results at the minimum threshold are listed in Table 2. For points above 1200 e, no η-correction is applied, since the application of the algorithm becomes challenging due to the small number of two-pixel clusters.

As the modifications to the n-implant are not applied in row direction, the spatial resolution for both pixel flavours agrees within the uncertainties. Although the resolution degrades with increasing threshold in agreement with the decrease in cluster size, the binary resolution of 8.7 µm is never exceeded. For high threshold values, an improvement of the spatial resolution is caused by the formation of inefficient regions at the pixel edges, as displayed in Fig. 7a. These inefficiencies lead to an effectively smaller pixel pitch that results in an artificial improvement in spatial resolution.

Within the uncertainties, the spatial resolution for the ≥ 50 µm thick sensors are in good agreement owing to the similar cluster size at a given threshold.

The 40 µm thick sensor performs worse for thresholds smaller than 1000 e owing to the smaller cluster size at a given threshold (cf. Fig. 3). For the flavour with continuous n-implant, the degradation is as high as 15 % at the minimum detection threshold. The difference vanishes at high thresholds, where cluster size one dominates for all sensor thicknesses.

The higher signal from the high-resistivity Czochralski sensors leads to a larger cluster size and consequently an improved spatial resolution. The difference is particularly noticeable at small threshold values in accordance with the larger difference in cluster size that was presented in Fig. 3b. At the minimum operation threshold listed in

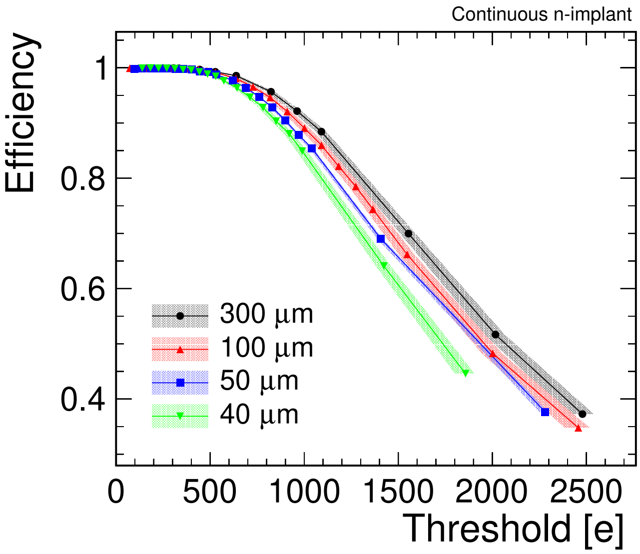

(a) Continuous n-implant

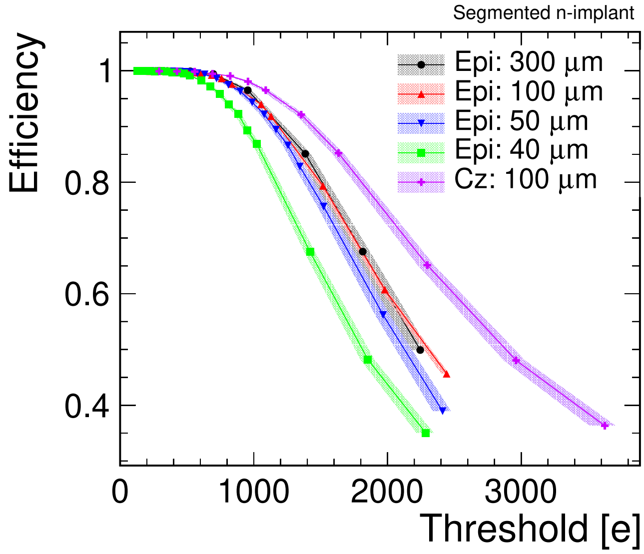

(b) Segmented n-implant

Figure 6: Hit detection efficiency as a function of the detection threshold using sensors with different sensor thicknesses and wafer materials for the pixel flavour with (a) continuous and (b) segmented n-implant using a bias voltage of -6 V/-6 V at the p-well/substrate.

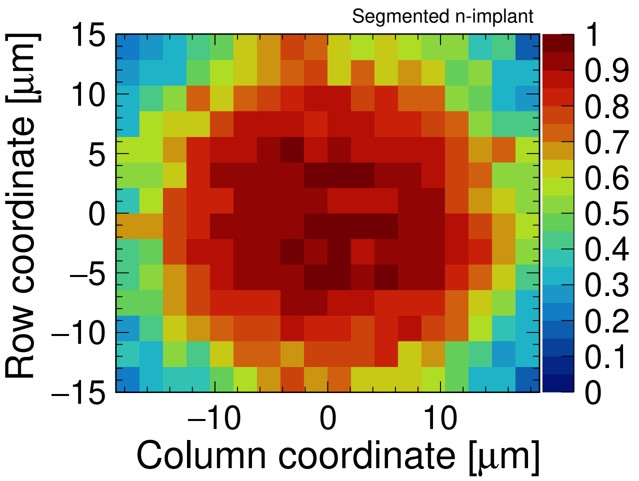

(a) Epitaxial layer

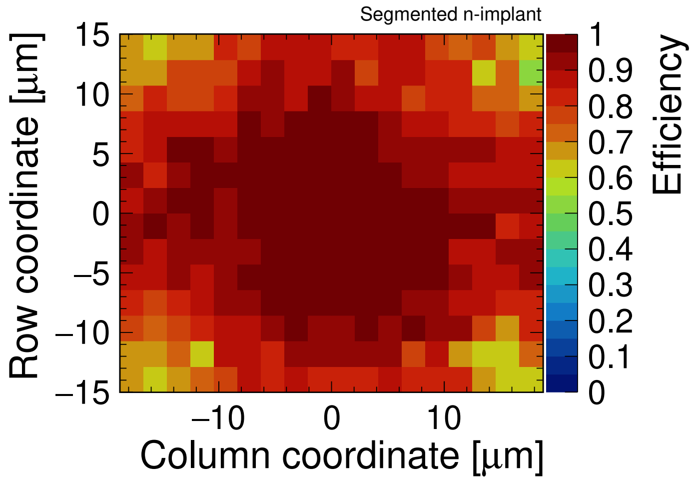

(b) High-resistivity Czochralski

Figure 7: In-pixel representation of the hit detection efficiency at the minimum operation threshold for a sensor with (a) epitaxial layer and (b) high-resistivity Czochralski substrate. Both sensors have a segmented n-implant and are biased at -6 V/-6 V at p-wells/substrate..

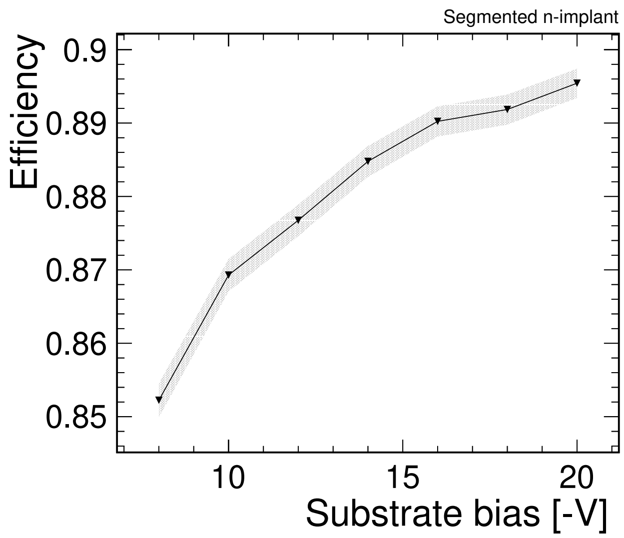

Figure 8: Hit detection efficiency as a function of the substrate bias voltage at a threshold of 1570 e for a high-resistivity Czochralski sample with segmented n-implant. The p-well voltage is fixed to -6 V.

Thickn. [µm]	**Mat.**	**Fl.**	**Thd.** [e]	**TR** [ns]
300	Epi	C	139^{+4}_{-5}	6.5 ± 0.1
100	Epi	C	136^{+4}_{-5}	6.4 ± 0.1
40	Epi	C	138^{+4}_{-5}	6.4 ± 0.1
300	Epi	S	136^{+4}_{-5}	5.6 ± 0.1
100	Epi	S	131^{+4}_{-5}	5.5 ± 0.1
40	Epi	S	130^{+4}_{-5}	5.3 ± 0.1
100	Cz	S	151^{+4}_{-5}	4.8 ± 0.1

Table 3: Time resolution (TR) at the minimum operation threshold (Thd.) for both pixel flavours (Fl.), different sensor thicknesses (Thickn.) and wafer materials (Mat.). C - continuous n-implant, S - segmented n-implant, Epi - epitaxial layer, Cz - high-resistivity Czochralski substrate.

Table 2, the resolution improves by about 15 %. At high thresholds, the mean cluster size converges to one resulting in an identical resolution within the uncertainties.

With increasing substrate bias voltage, the depleted region expands evoking a higher signal that leads to a larger cluster size and consequently an improved spatial resolution, as illustrated in Fig. 10 for a high-resistivity Czochralski sensor with segmented n-implant at a comparably high threshold of 226 e. Between -6 V and -20 V, the spatial resolution improves by approximately 13 %. While the comparably high threshold limits the absolute performance improvement, the potential of the high-resistivity Czochralski substrate is still distinguishable.

4.4. Time Resolution

The time resolution after time-walk correction is depicted in Fig. 11 as a function of the detection threshold for both pixel flavours. The results at the minimum operation threshold are listed in Table 3. With increasing threshold, the time resolution degrades owing to a stronger contribution of amplitude noise causing a time jitter. The jitter is inversely proportional to the slope of the signal at the threshold-crossing point, which flattens towards the peak of the signal.

It has been shown that the time resolution is mostly dominated by the front-end of the device [5], which overshadows sensor effects related to the device thickness. Nevertheless, a 10 % improvement is visible for the high-resistivity Czochralski sensor owing to a larger seed signal, which suppresses time jitter. An increase in substrate bias voltage leads to an additional improvement in time resolution, as presented in Fig. 12 at a threshold of 226 e. An improvement of about 9 % is distinguishable between -6 V and -20 V.

RA [°]	**CS (col.)**	**CS (row)**
0	1.46 ± 0.01	1.38 ± 0.01
50	2.19 ± 0.01	1.41 ± 0.01
70	3.78 ± 0.01	1.46 ± 0.01

Table 4: Cluster size (CS) for different rotation angles (RA) using a sensor with epitaxial layer and continuous n-implant operated at a threshold of approximately 150 e.

5. Studies with Inclined Particle Tracks

In the following, the sensor performance is assessed for inclined particle tracks and the active sensor depth is investigated.

5.1. Performance

In many HEP applications, particles enter the sensor under an oblique angle, due to e.g. mechanical rotation of detector modules or curled particle trajectories in a magnetic field. Therefore, the sensor performance for inclined particle tracks merits detailed investigation. Here, a 300 µm thick sensor with epitaxial layer and continuous n-implant is shown to exemplify the effects of the inclination angle on the sensor performance.

Cluster Size. The amount of active silicon traversed by particles is varied by inclining the sensor relative to the beam axis. For high inclination angles, particle tracks cross several adjacent pixel cells, giving rise to a larger cluster size as illustrated in Fig. 13 for a sensor tilted in row direction. The mean cluster size at the minimum detection threshold is listed in Table 4. A considerable increase in cluster size in row direction is distinguishable principally due to the geometrical effect of charge deposition in several pixel cells. Between 0° and 70°, the increase is as high as 250 % at the minimum operation threshold. The simultaneous increase in cluster size in column direction is consistent with an overall increase in the number of

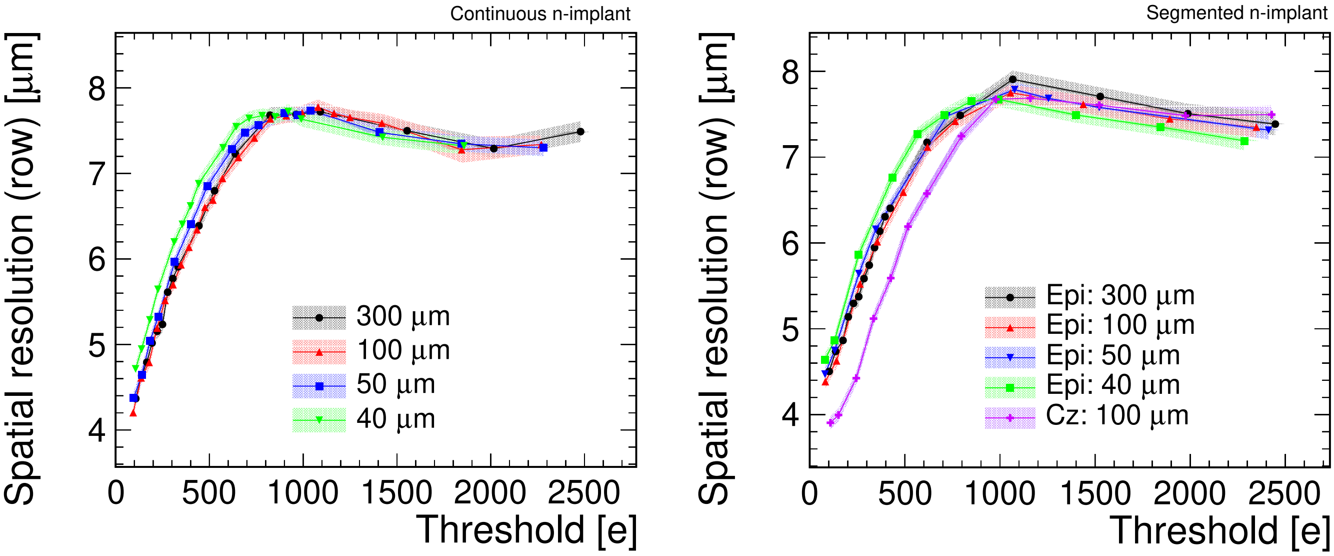

(a) Continuous n-implant

Figure 9: Spatial resolution as a function of the detection threshold using sensors with different thicknesses and wafer materials for the pixel flavour with (a) continuous and (b) segmented n-implant using a bias voltage of -6 V/-6 V at the p-well/substrate..

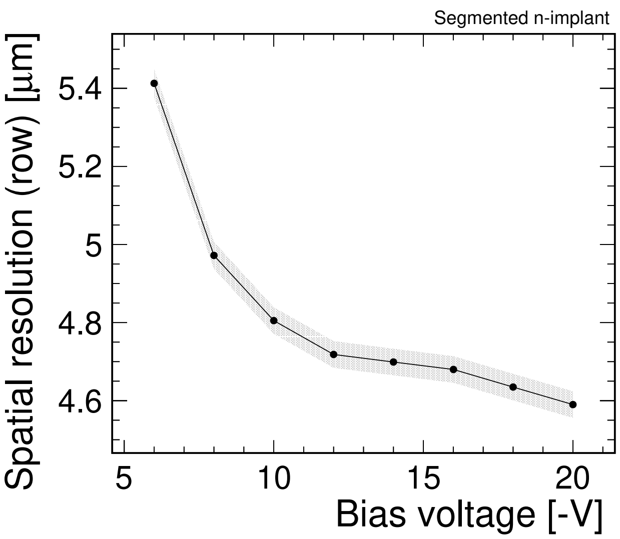

Figure 10: Spatial resolution as a function of the substrate bias voltage at a threshold of 226 e for a high-resistivity Czochralski sample with segmented n-implant. The p-well voltage is fixed to -6 V.

liberated charge carriers, whose undirected diffusion also affects charge sharing in column direction. At the minimum operation threshold, the mean cluster size in column direction is approximately 10 % larger at 70° compared to perpendicular incidence.

Efficiency. With increasing inclination angle, the total energy deposition in the sensor increases due to the longer particle path in the active sensor region. As a result, a higher signal is detected, which leads to an appreciable increase in efficiency at high thresholds, as depicted in Fig. 14, where the efficiency as a function of the detection threshold is shown for three different rotation angles. At a threshold of 2300 e, the increase in efficiency is approximately 75 % between 0° and 70°.

Spatial Resolution. The spatial resolution in row direction improves with increasing rotation angle until approximately 40°, where it evaluates to 3.6 ± 0.2 µm after η-correction, as illustrated in Fig. 15. The η-correction allows for an improvement in spatial resolution for rotation angles below 40°. At higher angles, an increase of cluster size ≥ 3 complicates the application of the reconstruction algorithms and no improvement with respect to the centre-of-gravity algorithm is achievable.

5.2. Determination of Active Sensor Depth

The extent of the active sensor volume is an essential ingredient to maximise the signal and thus optimise the sensor performance. The results from the previous sections imply that the active sensor volume only covers the upper part of the sensors with epitaxial layer, since thinning the devices down to 50 µm has no significant impact on the performance.

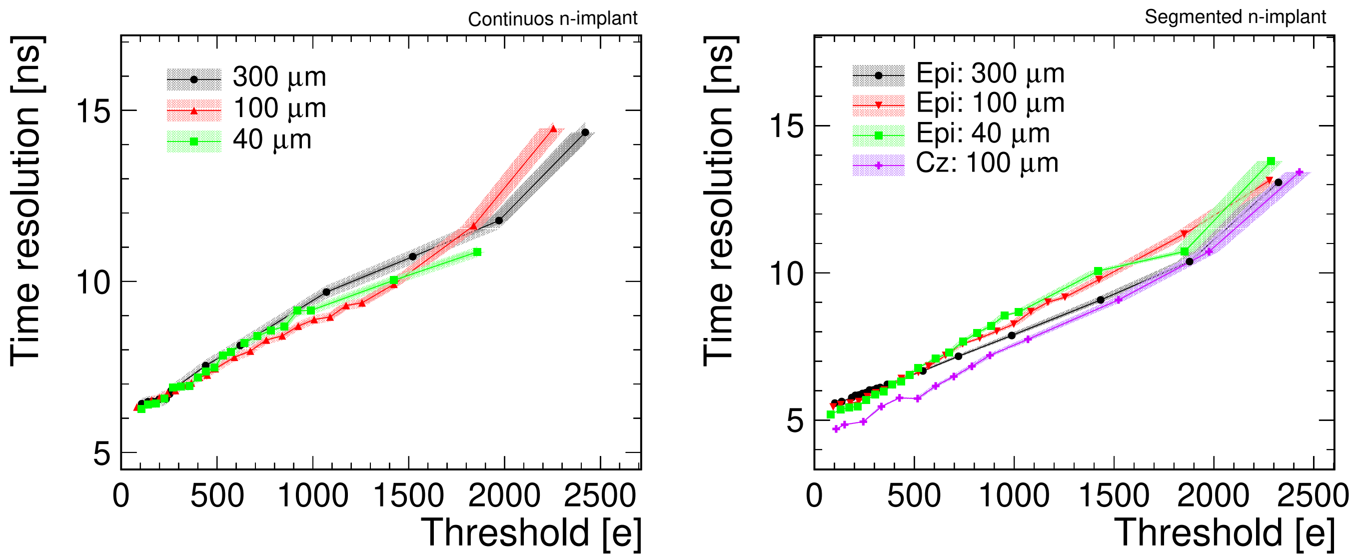

(a) Continuous n-implant

(b) Segmented n-implant

Figure 11: Time resolution as a function of the detection threshold using sensors with different thicknesses and wafer materials for the pixel flavour with (a) continuous and (b) segmented n-implant using a bias voltage of -6 V/-6 V at the p-well/substrate..

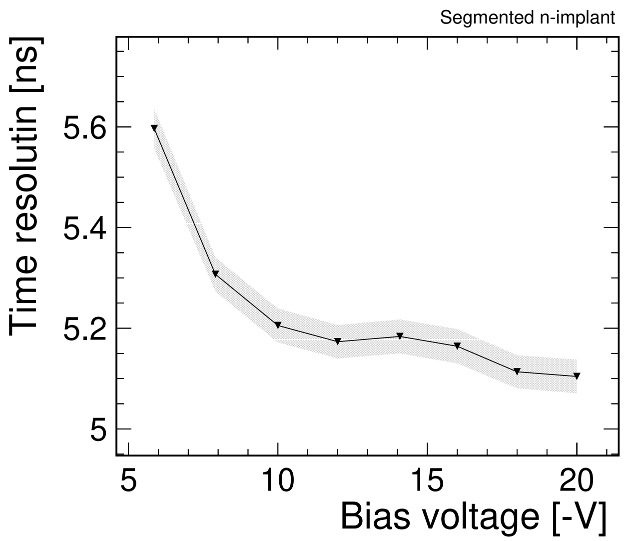

Figure 12: Time resolution as a function of the substrate bias voltage at a threshold of 226 e for a high-resistivity Czochralski sample with segmented n-implant. The p-well voltage is fixed to -6 V.

Fl.	**Thickn.** [µm]	**AD** [µm]
C	300	31.4 ± 0.1 (stat.)$^{+0.2}_{-2.4}$ (syst.)
C	100	30.7 ± 0.1 (stat.)$^{+0.3}_{-1.8}$ (syst.)
C	50	29.4 ± 0.1 (stat.)$^{+0.9}_{-1.0}$ (syst.)
C	40	26.2 ± 0.1 (stat.)$^{+0.8}_{-1.0}$ (syst.)
S	300	30.8 ± 0.2 (stat.)$^{+0.4}_{-1.2}$ (syst.)
S	50	29.8 ± 0.1 (stat.)$^{+0.6}_{-1.0}$ (syst.)

Table 5: Active depth (AD) for both pixel flavours (Fl.) and different sensor thicknesses (Thickn.).

To quantify the thickness of the active sensor volume, grazing angle measurements [8] are performed, whereby inclined particle tracks are used to determine an equivalent charge-collection depth for the observed cluster size.

The estimation of the active sensor depth is based on geometrical consideration, as sketched in Fig. 16. The model relates the cluster size in the tilt direction to the incident angle α and the active depth d. Charge carriers created below the active depth are assumed to have no effect on the cluster size. The following geometrical relation is considered to extract the active depth d for a sensor tilted in column direction:

$$\text{column cluster size} = \frac{d \tan \alpha}{\text{pitch}} + s_0, \tag{1}$$

where s_0 is the cluster column size for no rotation ($\alpha = 0$). The active depth is extracted with a linear fit to the mean cluster size as a function of the tangent of the rotation angle, as exemplified in Fig. 18 for the pixel flavour with continuous n-implant using sensors with different sensor

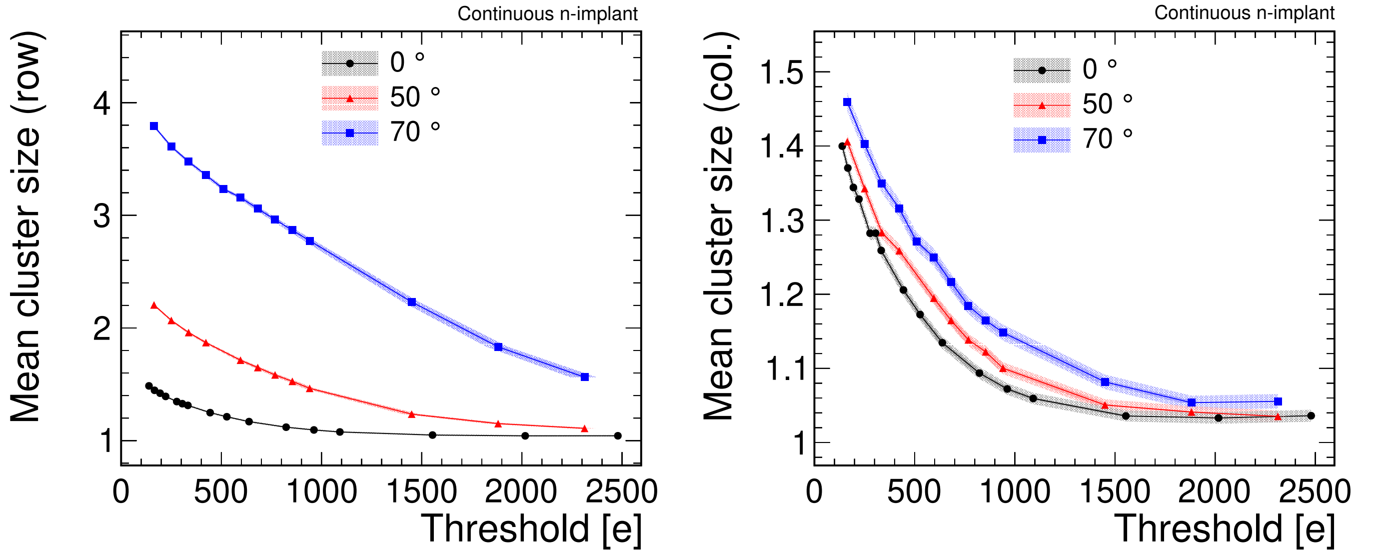

(a) Cluster size in row direction

(b) Cluster size in column direction

Figure 13: Cluster size as a function of the detection threshold for different rotation angles for a sensor with epitaxial layer and continuous n-implant tilted in row direction. A bias voltage of -6 V/-6 V is applied to the p-well/substrate.

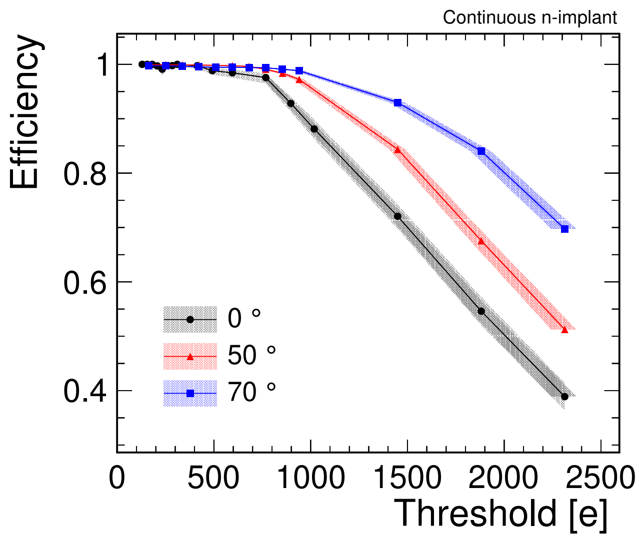

Figure 14: Detection efficiency as a function of the detection threshold for different rotation angles for a sensor with epitaxial layer and continuous n-implant. The sensor was tilted in row direction and the p-well/substrate was biased at -6 V/-6 V.

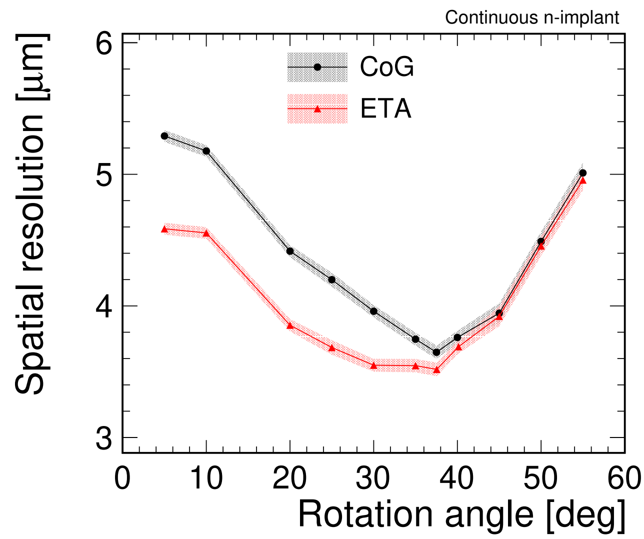

Figure 15: Spatial resolution as a function of the rotation angle using a charge-weighted centre-of-gravity algorithm (CoG) and an η-correction (ETA) to reconstruct the cluster position on the DUT. A bias voltage of -6 V/-6 V was applied to the p-well/substrate.

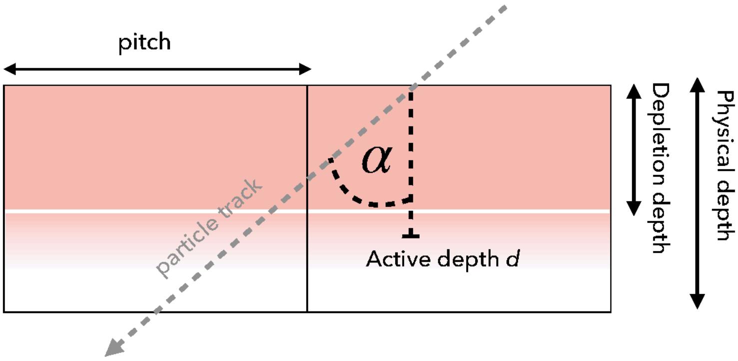

Figure 16: Schematic representation of the cluster size dependence on the inclination angle of the particle track.

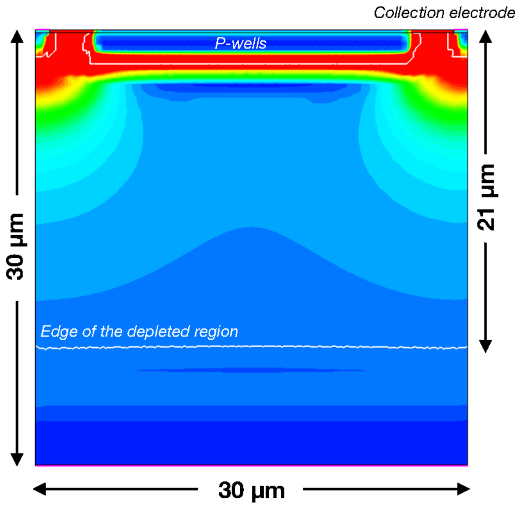

Figure 17: Two-dimensional cross section of the electric field simulated with 3D TCAD. Only the epitaxial layer is simulated for the pixel flavour with continuous n-implant. The edges of the depleted region are marked with a white line.

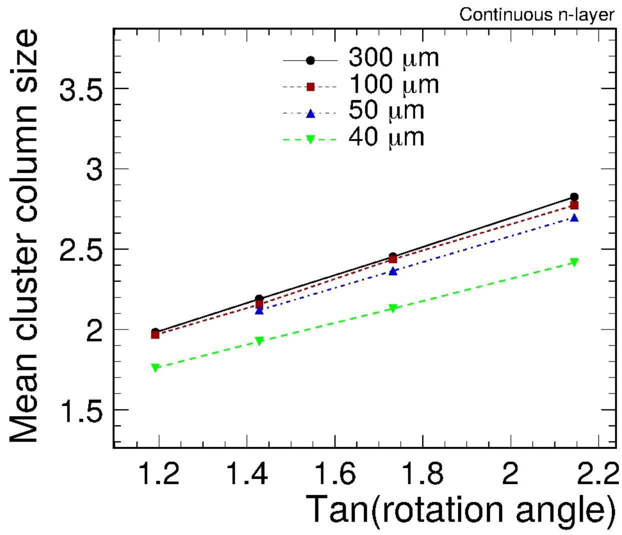

Figure 18: Cluster column size as a function of the tangent of the rotation angle for a sensor with epitaxial layer and continuous n-implant. A bias voltage of -6 V/-6 V was applied to the p-well/substrate.

thicknesses. The model neglects charge sharing that is not induced by rotation, i.e. charge sharing via diffusion is not accounted for. Since the cluster size at small rotation angles is dominated by diffusion effects, data points below 40° are excluded from the fit [26]. The effect of diffusion-induced charge sharing is considered in the systematic uncertainties by repeating the fit with varied fit ranges.

The fit results for both pixel flavours are summarised in Table 5. For all sensor types, the estimated active depth is larger than the depletion depth of 21 ± 1 µm expected from simulation studies, as illustrated in Fig. 17. A cross section of the electric field simulated with 3D TCAD is shown for the pixel flavour with continuous n-implant. The edges of the depleted volume are marked with white lines. A non-negligible contribution of charge carriers from the undepleted region is possible, since there is still a residual electric field below the depletion line, which is approximately seven times higher compared to the field at the boundary of the epitaxial layer.

The estimated active depth agrees well with the nominal thickness of the epitaxial layer, which indicates that charge carriers from the undepleted low-resistivity substrate are negligible due to their small lifetime. Only the active depth for the 40 µm sensor is clearly smaller compared to the other sensors, which is in agreement with the results from the previous sections, where the reduced signal was attributed to the removal of active material.

It can be concluded that the CLICTD sensors with an epitaxial layer of 30 µm can be thinned down to a total thickness of 50 µm without suffering from a significant loss in sensor performance. For thinner sensors, performance degradations emerge due to the removal or damage of the active sensor volume.

Unlike for sensors with epitaxial layer, the depletion for

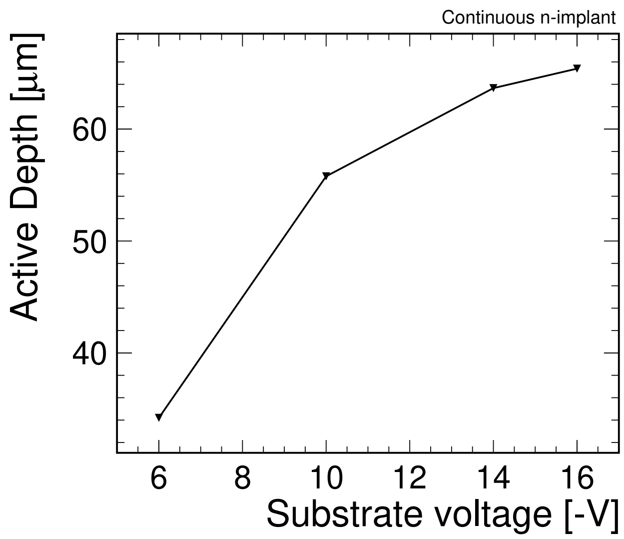

Figure 19: Active depth as a function of the substrate bias voltage for a sensor with high-resistivity Czochralski substrate with segmented n-implant.

the high-resistivity Czochralski wafers is not limited in depth by the thickness of the epitaxial layer. The increased depletion region gives access to a larger active sensor volume, as illustrated in Fig. 19, where the active depth as a function of the substrate voltage is depicted for a high-resistivity Czochralski sensor with segmented n-implant.

The active depth at a substrate voltage of -6 V evaluates to

$$34.2 \pm 0.1\ (\text{stat.})^{+1.5}_{-0.6}\ (\text{syst.})$$

and is therefore slightly larger compared to the sensors with epitaxial layer. With higher absolute substrate voltages, the active depth increases and reaches

$$65.4 \pm 0.1\ (\text{stat.})^{+0.5}_{-0.7}\ (\text{syst.})$$

at a substrate voltage of -16 V. At this voltage, the active depth is more than twice as large as the depth for the sensors with epitaxial layer and a corresponding increase in signal is expected. The higher signal translates into a better performance as shown in the previous section. However, the improvement is limited by the front-end, which is not optimised for the large signal generated in the high-resistivity material.

6. Summary & Outlook

The performance, charge sharing properties and the active sensor depth were investigated for the small collection-electrode monolithic CMOS sensor CLICTD. Different thicknesses for samples with a high-resistivity epitaxial layer were studied and the performance was found to be similar for sensors between 50 µm and 300 µm. Sensors thinned down to 40 µm exhibited a degradation in performance, which was attributed to a smaller active sensor depth as determined by grazing angle measurements. The active depth of the thicker sensors was found to correspond to the nominal thickness of 30 µm of the epitaxial layer itself.

To achieve a larger active depth and consequently a higher signal, CLICTD sensors fabricated on 100 µm thick high-resistivity Czochralski wafers were tested and a twofold increase in active depth was found using a substrate bias voltage of -16 V. As a consequence, an improvement of approximately 15 % in spatial and 10 % in time resolution was determined in combination with an improved efficiency at high detection thresholds. The improvement is limited by the front-end design that is not optimised for the high-resistivity Czochralski material, but could be improved in future designs.

The sensor performance was also evaluated for inclined particle tracks and an improved performance was found due to the longer particle path through the active sensor volume resulting in a higher signal. The spatial resolution has an optimum at an inclination angle of 40°, where it evaluates to 3.6 ± 0.2 µm after η-correction.

Acknowledgements

The authors would like to thank the STREAM network for providing the high-resistivity wafer material and coordinating the sensor production. The measurements leading to these results have been performed at the Test Beam Facility at DESY Hamburg (Germany), a member of the Helmholtz Association (HGF). This project has received funding from the European Union's Horizon 2020 research and innovation programme under grant agreement No 654168. This work has been sponsored by the Wolfgang Gentner Programme of the German Federal Ministry of Education and Research (grant no. 05E15CHA). This work was carried out in the framework of the CLICdp Collaboration.

CRediT authorship statement

R. Ballabriga Resources **J. Braach** Investigation **E. Buschmann** Investigation **M. Campbell** Methodology, Resources **D. Dannheim** Investigation, Methodology, Supervision, Writing - Review & Editing **K. Dort** Formal analysis, Investigation, Software, Visualization, Writing - Original Draft **L. Huth** Investigation, Software **I. Kremastiotis** Investigation, Resources **J. Kröger** Investigation, Software **L. Linssen** Project administration, Funding acquisition **M. Munker** Investigation, Methodology, Supervision **W. Snoeys** Conceptualization, Resources **S. Spannagel** Investigation, Software **P. Švihra** Writing - Review & Editing **T. Vanat** Investigation, Resources

References

[1] W. Snoeys, Monolithic pixel detectors for high energy physics, Nucl. Instr. Meth. A 731 (2013) 125 – 130. doi:10.1016/j.nima.2013.05.073.

[2] M. Mager, et al., ALPIDE, the Monolithic Active Pixel Sensor for the ALICE ITS upgrade, Nucl. Instr. Meth. A 824 (2016) 434–438.

[3] M. Dyndal, et al., Mini-MALTA: Radiation hard pixel designs for small-electrode monolithic CMOS sensors for the High Luminosity LHC, JINST 15 (02) (2020) P02005.

[4] T. Kugathasan, et al., Monolithic CMOS sensors for sub-nanosecond timing, Nucl. Instr. Meth. A 979 (2020) 164461.

[5] R. Ballabriga, et al., Test-beam characterisation of the CLICTD technology demonstrator - A small collection electrode high-resistivity CMOS pixel sensor with simultaneous time and energy measurement, Nucl. Instr. Meth. A 1006 (2021) 165396. doi:https://doi.org/10.1016/j.nima.2021.165396.

[6] W. Snoeys, et al., A process modification for CMOS monolithic active pixel sensors for enhanced depletion, timing performance and radiation tolerance, Nucl. Instr. Meth. A 871 (2017) 90 – 96. doi:10.1016/j.nima.2017.07.046.

[7] H. Pernegger, et al., Radiation hard monolithic CMOS sensors with small electrodes for High Luminosity LHC, Nucl. Instr. Meth. A 986 (2021) 164381.

[8] S. Meroli, D. Biagetti, D. Passeri, P. Placidi, L. Servoli, P. Tucceri, A grazing angle technique to measure the charge collection efficiency for CMOS active pixel sensors, Nucl. Instr. Meth. A 650 (1) (2011) 230–234.

[9] I. Kremastiotis, et al., Design and Characterization of the CLICTD Pixelated Monolithic Sensor Chip, IEEE Trans. Nucl. Sci. 67 (10) (2020) 2263–2272. doi:10.1109/TNS.2020.3019887.

[10] J. W. van Hoorne, Study and Development of a novel Silicon Pixel Detector for the Upgrade of the ALICE Inner Tracking System, PhD thesis, Technische Universität Wien (Nov 2015).
URL https://cds.cern.ch/record/2119197

[11] J. Prabket, et al., Resistivity profile of epitaxial layer for the new ALICE ITS sensor, JINST 14 (05) (2019) T05006.

[12] R. Diener, et al., The DESY II Test Beam Facility, Nucl. Instr. Meth. A 922 (2019) 265–286. doi:10.1016/j.nima.2018.11.133.

[13] J. Baudot, et al., First test results of MIMOSA-26, a fast CMOS sensor with integrated zero suppression and digitized output, 2009 IEEE Nucl Sci Symp Conf Rec (2009) 1169–1173.

[14] T. Poikela, et al., Timepix3: a 65k channel hybrid pixel readout chip with simultaneous ToA/ToT and sparse readout, JINST 9 (05) (2014) C05013–C05013. doi:10.1088/1748-0221/9/05/c05013.

[15] P. Baesso, D. Cussans, J. Goldstein, The AIDA-2020 TLU: a flexible trigger logic unit for test beam facilities, JINST 14 (09) (2019) P09019. doi:10.1088/1748-0221/14/09/P09019.

[16] Y. Liu, et al., EUDAQ2—A flexible data acquisition software framework for common test beams, JINST 14 (10) (2019) P10033. doi:10.1088/1748-0221/14/10/P10033.

[17] D. Dannheim, et al., Corryvreckan: A Modular 4D Track Reconstruction and Analysis Software for Test Beam Data, JINST 16 (03) (2021) P03008. doi:10.1088/1748-0221/16/03/p03008.

[18] J. Kröger, S. Spannagel, M. Williams, Corryvreckan User Manual, latest version.
URL http://cern.ch/go/db9Z

[19] K. Akiba, et al., Charged Particle Tracking with the Timepix ASIC, Nucl. Instrum. Meth. A 661 (2012) 31–49. doi:10.1016/j.nima.2011.09.021.

[20] V. Blobel, A new fast track-fit algorithm based on broken lines, Nucl. Instrum. Meth. A 566 (2006) 14–17. doi:10.1016/j.nima.2006.05.156.

[21] S. Spannagel, H. Jansen, Gbl track resolution calculator v2.0, 2016. doi:doi:10.5281/zenodo.48795.
URL https://github.com/simonspa/resolution-simulator

[22] H. Jansen, et al., Performance of the EUDET-type beam telescopes, EPJ Tech. Instrum. 3 (1) (2016) 7. doi:10.1140/epjti/s40485-016-0033-2.

[23] C. J. Clopper, E. S. Pearson, The use of confidence of fiducial limits illustrated in the case of the binomial, Biometrika 26 (4) (1934) 404–413. doi:10.1093/biomet/26.4.404.

[24] F. Pitters, et al., Time resolution studies of Timepix3 assemblies with thin silicon pixel sensors, JINST 14 (05) (2019) P05022. doi:10.1088/1748-0221/14/05/P05022.

[25] Y. Mizushima, et al., Impact of back-grinding-induced damage on Si wafer thinning for three-dimensional integration, Jpn. J. Appl. Phys. 53 (5S2) (2014) 05GE04.

[26] K. Dort, The CLICTD monolithic CMOS sensor, in: Proceedings of the 29th International Workshop on Vertex Detectors (VERTEX2020), 2021, p. 010019.